European Journal of Mechanics B/Fluids 42 (2013) 37–46

Contents lists available at ScienceDirect

European Journal of Mechanics B/Fluids

journal homepage: www.elsevier.com/locate/ejmflu

Buoyancy-driven mixing of multi-component fluids in two-dimensional tilted channels

Hyun Geun Lee, Junseok Kim *

Department of Mathematics, Korea University, Seoul 136-713, Republic of Korea

HIGHLIGHTS

- Buoyancy-driven mixing of multi-component fluids in tilted channels is studied numerically.
- The mixing dynamics are governed by the Navier–Stokes and multi-component Cahn–Hilliard equations.
- We numerically investigate the effects of various density ratios, tilt angles, Reynolds numbers, and Weber numbers.

ARTICLE INFO

Article history:
Received 20 January 2013
Received in revised form
19 May 2013
Accepted 9 June 2013
Available online 19 June 2013

Keywords:
Buoyancy-driven mixing
Multi-component fluid flows
Phase-field model
Inclined channel

ABSTRACT

Buoyancy-driven mixing of multi-component incompressible immiscible fluids in two-dimensional tilted channels is studied numerically using a phase-field model. This paper extends the previous work [K.C. Sahu, S.P. Vanka, A multiphase lattice Boltzmann study of buoyancy-induced mixing in a tilted channel, Comput. Fluids 50 (2011) 199–215] to the multi-component (more than two) fluid case. The mixing dynamics are governed by the modified Navier–Stokes equations and the multi-component convective Cahn–Hilliard equations. A finite difference method is used to discretize the governing system. To solve the equations efficiently and accurately, we employ Chorin's projection method for the modified Navier–Stokes equations, and the recently developed practically unconditionally stable method for the multi-component Cahn–Hilliard equations. We numerically investigate the effects of various density ratios, tilt angles, Reynolds numbers, and Weber numbers on the interface structures and front velocities. The trends observed in simulations with multi-component fluids are consistent with previous numerical results for two-component fluids.

1. Introduction

Buoyancy-driven mixing of multi-component fluids in a pipe or a channel of arbitrary inclination (including the vertical and horizontal) is a widespread phenomenon encountered in both natural (oceanography, hydrology, and atmospheric sciences) and industrial (chemical and petroleum engineering) systems [1–3]. A few examples of such mixing processes include the transportation of crude oil in pipelines [4], the propagation of fire through stairwells or ventilation ducts in buildings [5], and the mixing of fluids using centerline injectors [6].

Recently, buoyancy-driven mixing has been studied experimentally [7–12] and numerically [13–16]. In a series of papers [7–11], Séon and co-authors reported their experimental investigations of the lock-exchange problem [1,17,18], whereby a tilted cylindrical tube is filled with two-component fluids of different densities (the upper part is the heavier fluid) and a gate valve separating them is suddenly removed. As a result of buoyancy, the fluids interpenetrate and mix with each other.

Hallez and Magnaudet [13] conducted a numerical study of the effects of channel geometry on buoyancy-driven mixing using a finite volume method. They considered four different geometries: a two-dimensional channel, a cylindrical tube, a square duct with four no-slip walls, and a square duct with two no-slip walls and two periodic lateral walls. The authors showed that the vortices that develop during the evolution of the flow are more coherent and persistent in two than in three dimensions. They also observed that the two-dimensional vortices can tear off the head of the current and separate it from the body. In contrast, such separations are only temporary in square channels, and never occur in a cylindrical tube.

Sahu et al. [14] examined the characteristics of pressure-driven two-fluid flow in two-dimensional inclined channels with density and viscosity contrasts using numerical simulations. They investigated the effects of the density ratio, Froude number, and channel inclination on the flow dynamics for moderate Reynolds numbers and viscosity ratios. The authors observed that the rates of mixing and displacement of the more viscous fluid are enhanced with

* Corresponding author. Tel.: +82 2 3290 3077; fax: +82 2 929 8562.
E-mail address: cfdkim@korea.ac.kr (J. Kim).
URL: http://math.korea.ac.kr/~cfdkim (J. Kim).

0997-7546/$ – see front matter
http://dx.doi.org/10.1016/j.euromechflu.2013.06.004

increasing density ratio and Froude number. They also found that these rates increase with increasing inclination angles (measured from the horizontal).

Sahu and Vanka [15] studied the effects of density ratios, Reynolds numbers, tilt angles, and surface tension parameters on the buoyancy-induced interpenetration of two immiscible fluids in a two-dimensional tilted channel using a two-phase lattice Boltzmann method. Their results were in good agreement with the finite volume solutions generated with the code used by Sahu et al. [14] and exhibited similar trends to the experiments of Séon et al. [7–11]. Redapangu et al. [16] studied the effects of the viscosity difference in the same situation. Relatively stable fingers were observed for high viscosity ratios, with the flow essentially becoming two individual Poiseuille flows.

Most experimental and numerical studies of buoyancy-driven mixing have been performed for two-component fluids. However, many problems in real-world applications relate to the mixing of multi-component fluids. For example, a correct understanding of three-component fluid flow (oil/gas/water) is crucial in petroleum engineering for the design of efficient recovery techniques. Therefore, this paper is concerned with the mixing of multi-component (more than two) fluids. In the present paper, we extend the previous work of Sahu and Vanka [15] to the multi-component fluid case using a phase-field model [19,20]. We are particularly interested in evaluating the effects of parameters such as the density ratio, tilt angle, Reynolds number, and Weber number. The mixing dynamics are governed by the modified Navier–Stokes equations and the multi-component convective Cahn–Hilliard equations [21–26]. We discretize the governing system using a finite difference method. To solve the equations efficiently and accurately, we employ Chorin's projection method [27] for the modified Navier–Stokes equations, and the recently developed practically unconditionally stable method for the multi-component Cahn–Hilliard equations [26].

The paper is organized as follows. In Section 2, we present the governing equations that describe the buoyancy-driven mixing of multi-component fluids. In Section 3, a numerical solution is given. We perform some characteristic numerical experiments for two- and four-component fluids in Section 4, before drawing our conclusions in Section 5.

2. Governing equations

We consider the flow of N incompressible immiscible fluids in a two-dimensional channel, inclined at an angle θ to the vertical. A schematic illustration of the initial fluid configuration is shown in Fig. 1. x and y denote the axial and transverse coordinates, respectively, and L and H are the length and height of the channel, respectively. Fluids 1 and N are the heaviest and lightest fluids, respectively, and the heavier fluids are initially above the lighter fluids in a gravitational field. Let $\mathbf{c} = (c_1, c_2, \ldots, c_N)$ be a vector-valued phase-field, where each order parameter c_k is the concentration of each component in the mixture. In order to investigate the multiphase fluid flow characteristics, we couple the modified Navier–Stokes equations and the N-component convective Cahn–Hilliard equations:

$$\rho(\mathbf{c})\left(\frac{\partial \mathbf{u}}{\partial t} + \mathbf{u}\cdot\nabla\mathbf{u}\right) = -\nabla p + \nabla\cdot\left[\eta(\mathbf{c})(\nabla\mathbf{u} + \nabla\mathbf{u}^T)\right] + \mathbf{SF}(\mathbf{c}) + \rho(\mathbf{c})\mathbf{g}, \tag{1}$$

$$\nabla\cdot\mathbf{u} = 0, \tag{2}$$

$$\frac{\partial c_k}{\partial t} + \nabla\cdot(c_k\mathbf{u}) = \nabla\cdot(M(\mathbf{c})\nabla\mu_k), \tag{3}$$

$$\mu_k = f(c_k) - \epsilon^2\Delta c_k + \beta_k, \quad \text{for } k = 1, 2, \ldots, N, \tag{4}$$

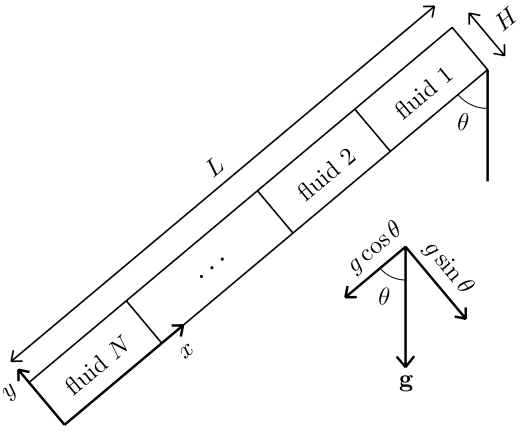

Fig. 1. Schematic illustration of the initial fluid configuration. x and y denote the axial and transverse coordinates, respectively, and the two-dimensional channel is inclined at an angle θ to the vertical. Fluids 1 and N are the heaviest and lightest fluids, respectively, and heavier fluids are initially above lighter fluids in a gravitational field.

where $\rho(\mathbf{c})$ is the variable density, $\mathbf{u}$ is the fluid velocity, p is the pressure, $\eta(\mathbf{c})$ is the variable viscosity, $\mathbf{SF}(\mathbf{c})$ is the surface tension force, $\mathbf{g} = (-g\cos\theta, -g\sin\theta)$ is the gravity term under gravitational acceleration g, $M(\mathbf{c})$ is a mobility, $f(c_k) = c_k(c_k - 0.5)(c_k - 1)$, ϵ is a positive constant, and $\beta_k = -c_k\sum_{j=1}^{N} f(c_j)$. $\rho(\mathbf{c})$ and $\eta(\mathbf{c})$ are defined as $\rho(\mathbf{c}) = \sum_{k=1}^{N}\rho_k c_k$ and $\eta(\mathbf{c}) = \sum_{k=1}^{N}\eta_k c_k$, where ρ_k and η_k are the density and viscosity of the kth fluid, respectively. For the surface tension force $\mathbf{SF}(\mathbf{c})$, we use the generalized continuous surface tension force formulation [24]: $\mathbf{SF}(\mathbf{c}) = \sum_{i=1}^{N-1}\left(\sum_{j=i+1}^{N} 0.5\sigma_{ij}[\mathbf{sf}(c_i) + \mathbf{sf}(c_j)]\delta(c_i, c_j)\right)$, where σ_{ij} is the physical surface tension coefficient between fluid i and fluid j, $\mathbf{sf}(c_i) = -6\sqrt{2}\epsilon\nabla\cdot(\nabla c_i/|\nabla c_i|)|\nabla c_i|\nabla c_i$, and $\delta(c_i, c_j) = 5c_i c_j$. For a large density ratio, the continuity equation cannot be reduced to Eq. (2). In such cases, we should use $\rho_t + \nabla\cdot(\rho\mathbf{u}) = 0$ as the continuity equation. In [28], Ding et al. discussed this issue and derived a set of equations from the conservation law of the mass of binary mixtures. $M(\mathbf{c})$ in Eq. (3) is treated as a variable mobility in [28–34], and the Cahn–Hilliard equation has been extensively employed with a constant mobility [35–41]. In this paper, we take the mobility to be constant ($M(\mathbf{c}) \equiv M$), as a variable mobility is computationally more expensive.

To non-dimensionalize the governing equations (1)–(4), we define characteristic quantities of length (L_c), velocity (U_c), density (ρ_c), viscosity (η_c), and chemical potential (μ_c). In our simulations, we choose $L_c = H$, $U_c = \sqrt{gH}$, $\rho_c = \rho_N$, and $\eta_c = \eta_N$. We then introduce the following dimensionless variables:

$$\mathbf{x}' = \frac{\mathbf{x}}{L_c}, \quad \mathbf{u}' = \frac{\mathbf{u}}{U_c}, \quad t' = \frac{tU_c}{L_c}, \quad \rho' = \frac{\rho}{\rho_c},$$
$$p' = \frac{p}{\rho_c U_c^2}, \quad \eta' = \frac{\eta}{\eta_c}, \quad \mathbf{g}' = \frac{\mathbf{g}}{g}, \quad {\mu_k}' = \frac{\mu_k}{\mu_c},$$

where the primed quantities are dimensionless. Substituting these variables into Eqs. (1)–(4) and dropping the primes, we have

$$\rho(\mathbf{c})\left(\frac{\partial \mathbf{u}}{\partial t} + \mathbf{u}\cdot\nabla\mathbf{u}\right) = -\nabla p + \frac{1}{Re}\nabla\cdot\left[\eta(\mathbf{c})(\nabla\mathbf{u} + \nabla\mathbf{u}^T)\right] + \mathbf{SF}(\mathbf{c}) + \frac{\rho(\mathbf{c})}{Fr^2}\mathbf{g}, \tag{5}$$

$$\nabla\cdot\mathbf{u} = 0, \tag{6}$$

$$\frac{\partial c_k}{\partial t} + \nabla\cdot(c_k\mathbf{u}) = \frac{1}{Pe}\Delta\mu_k, \tag{7}$$

$$\mu_k = f(c_k) - \epsilon^2\Delta c_k + \beta_k, \quad \text{for } k = 1, 2, \ldots, N, \tag{8}$$

where $\mathbf{SF}(\mathbf{c}) = \sum_{i=1}^{N-1}(\sum_{j=i+1}^{N} 0.5[\mathbf{sf}(c_i) + \mathbf{sf}(c_j)]\delta(c_i, c_j)/We_{ij})$, $\mathbf{g} = (-\cos\theta, -\sin\theta)$, and ϵ is redefined according to the scaling. The dimensionless parameters are the Reynolds number, $Re = \rho_c U_c L_c/\eta_c$, the Weber number of fluids i and j, $We_{ij} = \rho_c L_c U_c^2/\sigma_{ij}$, the Froude number, $Fr = U_c/\sqrt{gL_c}$, and the Péclet number, $Pe = U_c L_c/(M\mu_c)$.

2.1. Boundary conditions

The accurate implementation of boundary conditions is an important issue associated with the direct numerical simulation of buoyancy-driven mixing processes. The boundary conditions employed in this paper are as follows.

Order parameter c_k. The previously used boundary condition for the concentration [14] and the index function [15] (in the phase-field method, these variables correspond to an order parameter c_k) is the zero Neumann boundary condition. However, this boundary condition means that the contact angle of the fluid interface is 90° at the walls. Thus, this boundary condition does not preserve the tilt angle near the boundary. In order to resolve this problem, we use the linear boundary condition for order parameters c_k:

$$\begin{aligned}\frac{\partial^2 c_k}{\partial x^2}(0, y, t) &= \frac{\partial^2 c_k}{\partial x^2}(L/H, y, t) = \frac{\partial^2 c_k}{\partial y^2}(x, 0, t)\\ &= \frac{\partial^2 c_k}{\partial y^2}(x, 1, t) = 0 \quad \text{for } 0 \le x \le L/H,\\ &\quad 0 \le y \le 1,\ 0 \le t \le T.\end{aligned}$$

Chemical potential μ_k. Because we are also interested in long-time simulations, mass conservation is an important factor. For mass conservation, we use the zero Neumann boundary condition: $\nabla\mu_k \cdot \mathbf{n} = 0$ on $\partial\Omega$, where $\mathbf{n}$ is the unit normal vector to $\partial\Omega$.

Velocities. No-slip boundary conditions are imposed: $\mathbf{u} = \mathbf{0}$ on $\partial\Omega$.

Pressure. Taking the inner product of both sides of Eq. (5) with $\mathbf{n}$, we have the boundary condition for the pressure:

$$\mathbf{n} \cdot \nabla p = \mathbf{n} \cdot \left(\frac{1}{Re}\nabla \cdot \left[\eta(\mathbf{c})(\nabla\mathbf{u} + \nabla\mathbf{u}^T)\right] + \mathbf{SF}(\mathbf{c}) + \frac{\rho(\mathbf{c})}{Fr^2}\mathbf{g}\right).$$

Owing to the treatment of pressure on the boundary, we can perform long-time evolutions resulting in an equilibrium state [42].

3. Numerical solution

Let the computational domain be partitioned into a uniform mesh with mesh spacing h. The center of each cell, Ω_{ij}, is located at $(x_i, y_j) = ((i - 0.5)h, (j - 0.5)h)$ for $i = 1, \ldots, N_x$ and $j = 1, \ldots, N_y$. N_x and N_y denote the number of cells in the x- and y-directions, respectively. Cell vertices are located at $(x_{i+\frac{1}{2}}, y_{j+\frac{1}{2}}) = (ih, jh)$. In this paper, the fluid variables are defined on a staggered grid [43]; pressures and vector-valued phase-fields are stored at the cell centers and velocities at cell faces.

To solve the modified Navier–Stokes equation, we apply the projection method [27], which decouples the solution of the momentum equations from the solution of the continuity equation. Let Δt be the time step and n be the time step index. At the beginning of each time step, given $\mathbf{u}^n$ and $\mathbf{c}^n$, we want to find $\mathbf{u}^{n+1}$, $\mathbf{c}^{n+1}$, and p^{n+1} that solve the following temporal discretization of Eqs. (5)–(8):

$$\begin{aligned}\rho^n\frac{\mathbf{u}^{n+1} - \mathbf{u}^n}{\Delta t} &= -\nabla_d p^{n+1} + \frac{1}{Re}\nabla_d \cdot \left[\eta^n(\nabla_d\mathbf{u}^n + (\nabla_d\mathbf{u}^n)^T)\right]\\ &\quad + \mathbf{SF}^n + \frac{\rho^n}{Fr^2}\mathbf{g} - \rho^n(\mathbf{u} \cdot \nabla_d\mathbf{u})^n,\end{aligned}$$

$$\nabla_d \cdot \mathbf{u}^{n+1} = 0,$$

$$\frac{{c_k}^{n+1} - {c_k}^n}{\Delta t} = \frac{1}{Pe}\Delta_d{\mu_k}^{n+1} - \nabla_d \cdot (c_k\mathbf{u})^n, \quad \text{for } k = 1, 2, \ldots, N-1, \tag{9}$$

$${\mu_k}^{n+1} = \varphi({c_k}^{n+1}) - 0.25{c_k}^n - \epsilon^2\Delta_d{c_k}^{n+1} + {\beta_k}^n, \tag{10}$$

where $\rho^n = \rho(\mathbf{c}^n)$, $\eta^n = \eta(\mathbf{c}^n)$, $\mathbf{SF}^n = \mathbf{SF}(\mathbf{c}^n)$, and $\varphi(c_k) = f(c_k) + 0.25c_k$ is a nonlinear function. Note that we need only solve these equations for $c_1, c_2, \ldots, c_{N-1}$, as $c_N = 1 - \sum_{k=1}^{N-1} c_k$. An outline of the main procedures in each time step is as follows.

Step 1. Initialize $\mathbf{u}^0$ to be the divergence-free velocity field and ${c_k}^0$ for $k = 1, 2, \ldots, N-1$.

Step 2. Solve an intermediate velocity field, $\tilde{\mathbf{u}}$:

$$\begin{aligned}\frac{\tilde{\mathbf{u}} - \mathbf{u}^n}{\Delta t} &= \frac{1}{\rho^n Re}\nabla_d \cdot \left[\eta^n(\nabla_d\mathbf{u}^n + (\nabla_d\mathbf{u}^n)^T)\right] + \frac{1}{\rho^n}\mathbf{SF}^n\\ &\quad + \frac{1}{Fr^2}\mathbf{g} - (\mathbf{u} \cdot \nabla_d\mathbf{u})^n,\end{aligned}$$

where the convective term, $(\mathbf{u} \cdot \nabla_d\mathbf{u})^n$, is computed using an upwind scheme [42]. We then solve the following equations for the advanced pressure field at $(n+1)$ time step:

$$\frac{\mathbf{u}^{n+1} - \tilde{\mathbf{u}}}{\Delta t} = -\frac{1}{\rho^n}\nabla_d p^{n+1}, \tag{11}$$

$$\nabla_d \cdot \mathbf{u}^{n+1} = 0.$$

Apply the divergence operator to Eq. (11) and get a Poisson equation for p^{n+1}:

$$\nabla_d \cdot \left(\frac{1}{\rho^n}\nabla_d p^{n+1}\right) = \frac{1}{\Delta t}\nabla_d \cdot \tilde{\mathbf{u}}. \tag{12}$$

The resulting linear system of Eq. (12) is solved by a fast solver, such as a linear multigrid method [44]. The divergence-free velocities are then defined by

$$\mathbf{u}^{n+1} = \tilde{\mathbf{u}} - \frac{\Delta t}{\rho^n}\nabla_d p^{n+1}.$$

Step 3. Update the phase-field ${c_k}^n$ to ${c_k}^{n+1}$ for $k = 1, 2, \ldots, N-1$. In order to solve the N-component Cahn–Hilliard system (9) and (10) in a decoupled way and reduce the CPU time and memory requirements, we use the recently developed practically unconditionally stable scheme [26]. For mass conservation, we use a conservative discretization of the convective part of the phase-field Eq. (9):

$$\begin{aligned}&\left[(c_k u)_x + (c_k v)_y\right]_{ij}^n\\ &= \frac{u^n_{i+\frac{1}{2},j}({c_k}^n_{i+1,j} + {c_k}^n_{ij}) - u^n_{i-\frac{1}{2},j}({c_k}^n_{ij} + {c_k}^n_{i-1,j})}{2h}\\ &\quad + \frac{v^n_{i,j+\frac{1}{2}}({c_k}^n_{i,j+1} + {c_k}^n_{ij}) - v^n_{i,j-\frac{1}{2}}({c_k}^n_{ij} + {c_k}^n_{i,j-1})}{2h}.\end{aligned}$$

This completes the single time-step process.

4. Numerical experiments

In this section, we describe a number of numerical experiments for two- and four-component fluids in two-dimensional tilted channels. We consider the long-time evolution of two-component fluids, compare the results with those obtained by a lattice Boltzmann method, and study the effects of Péclet number, density ratio, tilt angle, Reynolds number, Weber number, and channel aspect ratio. We also compare the mixing of two- and four-component fluids with the same maximum density contrast, and investigate the mixing of initially partly stable configurations for four-component fluids. For each experiment, the fluid viscosities

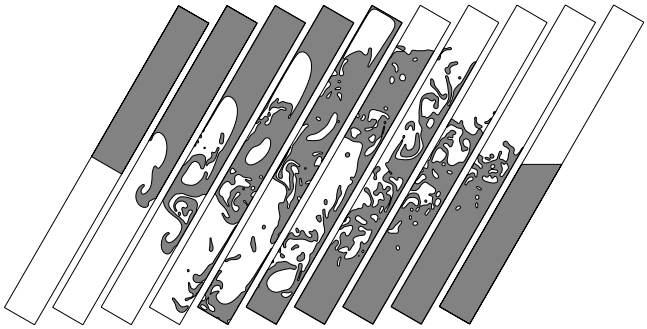

Fig. 2. Long-time evolution of two-component fluids in a two-dimensional tilted channel of aspect ratio 1 : 10 for $\rho_1/\rho_2 = 3$, $\theta = 30^\circ$, $Re = 3000$, and $We = \infty$. The heavier and lighter fluids are represented by gray and white colors, respectively. The times are $t = 0$, 3, 7, 12, 18, 25, 40, 50, 60, and 90 (from left to right).

are matched. In the case of four-component fluids, we take the same value (We) for all Weber numbers, i.e., $We_{ij} = We$. Throughout the rest of this section, we use the notation $We = \infty$ for the zero surface tension case and take the filled contour of the 0.5 level of each phase-field to capture the fluid interfaces.

4.1. Buoyancy-driven mixing of two-component fluids in two-dimensional tilted channels

4.1.1. Long-time evolution of two-component fluids in a two-dimensional tilted channel

We validate our code by simulating the long-time evolution of two-component fluids in a two-dimensional tilted channel. The initial conditions are

$$c(x, y, 0) = \frac{1}{2}\left(1 + \tanh\left(\frac{x-5}{2\sqrt{2}\epsilon}\right)\right),$$
$$u(x, y, 0) = v(x, y, 0) = 0$$

on the domain $\Omega = [0, 10] \times [0, 1]$. Here, we use $h = 1/64$, $\Delta t = 0.128h$, $\epsilon = 0.01\sqrt{2}$, and $Pe = 1/\epsilon$. The remaining parameter values are $\rho_1/\rho_2 = 3$, $\theta = 30^\circ$, $Re = 3000$, and $We = \infty$. We continue the simulation until the solution becomes numerically stationary. Fig. 2 shows the evolution of the phase-field; the heavier and lighter fluids are represented by gray and white colors, respectively. As we can see in Fig. 2, the heavier and lighter fluids move along the lower ($y = 0$) and upper ($y = 1$) walls, respectively, due to the gravitational force. Rayleigh–Taylor-type instabilities occur in both the x- and y-directions, because the gravitational force has x- and y-components that are proportional to $g\cos\theta$ and $g\sin\theta$, respectively. With time, the development of instabilities produces a wavy interface between the two fluids, leading to the formation of vortical patterns. Finally, after $t = 90$, the system reaches an equilibrium state: the heavier fluid is completely below the lighter fluid, and the interface is flat and perpendicular to the gravitational direction.

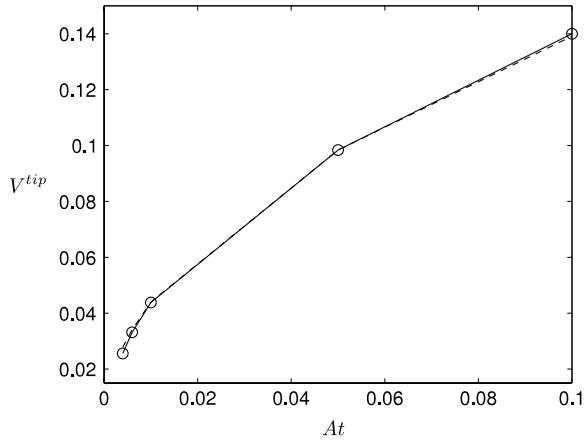

Fig. 4. Variation in front velocity of the heavier fluid for $At = 0.004$, 0.006, 0.01, 0.05, and 0.1. $\theta = 30^\circ$, $Re = 558.6$, and $We = \infty$ are used. The dashed line in this plot corresponds to $0.44\sqrt{gHAt}$.

4.1.2. Comparison with lattice Boltzmann results

To compare the results of our phase-field simulation with those obtained by a lattice Boltzmann method [15], we first consider the following initial data:

$$c(x, y, 0) = \frac{1}{2}\left(1 + \tanh\left(\frac{x-20}{2\sqrt{2}\epsilon}\right)\right), \tag{13}$$

$$u(x, y, 0) = v(x, y, 0) = 0 \tag{14}$$

on the domain $\Omega = [0, 40] \times [0, 1]$, with $h = 1/64$, $\Delta t = 0.128h$, $\epsilon = 0.01\sqrt{2}$, and $Pe = 100/\epsilon$. The remaining parameter values are $\rho_1/\rho_2 = 1.2$, $\theta = 60^\circ$, $Re = 558.6$, and $We = \infty$. Fig. 3 shows the evolution of the phase-field obtained by a phase-field method and the density contour obtained by a lattice Boltzmann method at $t = 10$ and 20. The heavier and lighter fluids are shown as red and blue, respectively. As we can see, these results are in good qualitative agreement for a typical set of parameters.

We next examine the Atwood number ($At = (\rho_1 - \rho_2)/(\rho_1 + \rho_2)$) dependence of the front velocity of the heavier fluid for the problem presented in Section 4.1 of Ref. [15]. We take the initial data given in Eqs. (13) and (14), and choose $h = 1/64$, $\Delta t = 0.128h$, $\epsilon = 0.01\sqrt{2}$, $Pe = 100/\epsilon$, $\theta = 30^\circ$, $Re = 558.6$, and $We = \infty$. The variation in front velocity of the heavier fluid for $At = 0.004$, 0.006, 0.01, 0.05, and 0.1 is shown in Fig. 4. Note that, in [15], the authors found that the front velocity of the heavier fluid increases as a function of $\sqrt{gHAt}$ (the constant of proportionality is 0.38) for Atwood numbers less than 0.06. However, for Atwood numbers greater than 0.06, no dependence on $\sqrt{gHAt}$ was observed, and instead a smaller growth rate appeared. The authors believed this may be due to the increased nonlinearities causing an enhanced diffusion of the density interface. This in turn reduces the driving potential for the finger velocities, thus reducing the generated slope. However, in our simulation, we see a $\sqrt{gHAt}$ dependence for all given Atwood numbers, with a constant of proportionality of 0.44.

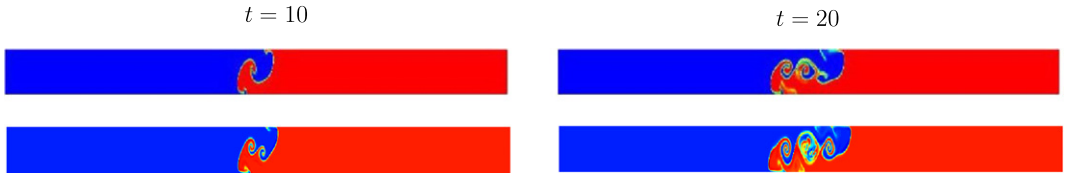

Fig. 3. Comparison with lattice Boltzmann results. Bottom: phase-field obtained by a phase-field method for a channel of aspect ratio 1 : 40. The remaining parameter values are $\rho_1/\rho_2 = 1.2$, $\theta = 60^\circ$, $Re = 558.6$, and $We = \infty$. The heavier and lighter fluids are shown in red and blue, respectively. (For interpretation of the references to colour in this figure legend, the reader is referred to the web version of this article.)
Source: Top: Reprinted from [15], with permission from Elsevier.

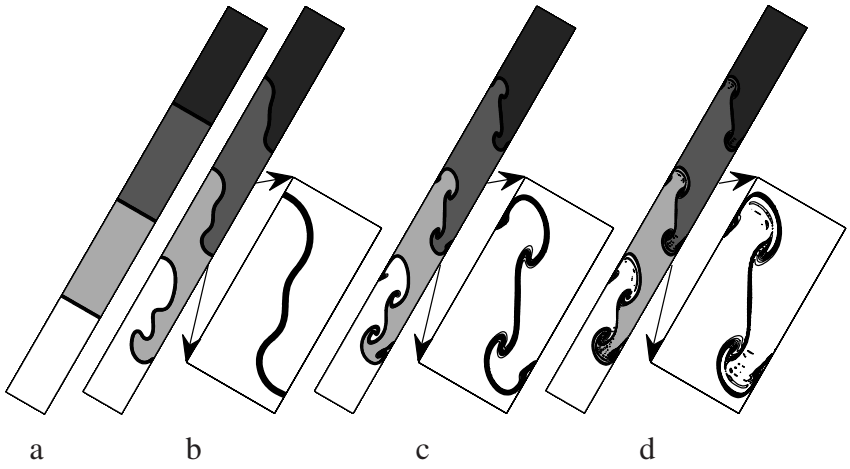

Fig. 5. Effect of Péclet number on the evolution of the interface. (a) Shows the initial configuration. (b), (c), and (d) are snapshots of the interface profile at $t = 4$ for $Pe = 0.01/\epsilon$, $1/\epsilon$, and $100/\epsilon$, respectively. Next to each figure, the magnification shows the contour lines of the phase-field c_2 at levels 0.1, 0.2, ..., 0.9. $\theta = 30^\circ$, $\rho_1 : \rho_2 : \rho_3 : \rho_4 = 4 : 3 : 2 : 1$, $Re = 3000$, and $We = \infty$ are used. Fluids 1, 2, 3, and 4 are represented by black, dark gray, gray, and white, respectively.

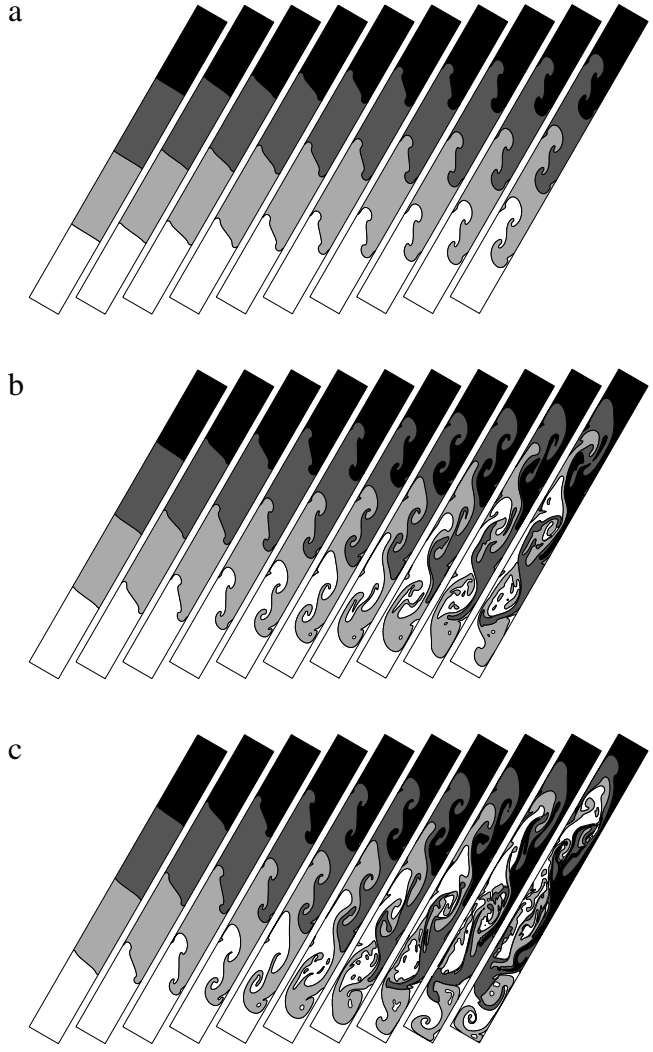

Fig. 6. Effect of density ratio on the evolution of four-component fluids. The density ratio between the fluids is taken to be $\rho_1 : \rho_2 : \rho_3 : \rho_4 = (1 + 3m) : (1 + 2m) : (1 + m) : 1$ for the parameter m. (a), (b), and (c) are the results for $m = 0.1$, 0.5, and 1, respectively. The other parameters are $\theta = 30^\circ$, $Re = 3000$, and $We = \infty$. The times are $t = 1, 2, 3, 4, 5, 6, 7, 8, 9$, and 10 (from left to right). Fluids 1, 2, 3, and 4 are represented by black, dark gray, gray, and white, respectively.

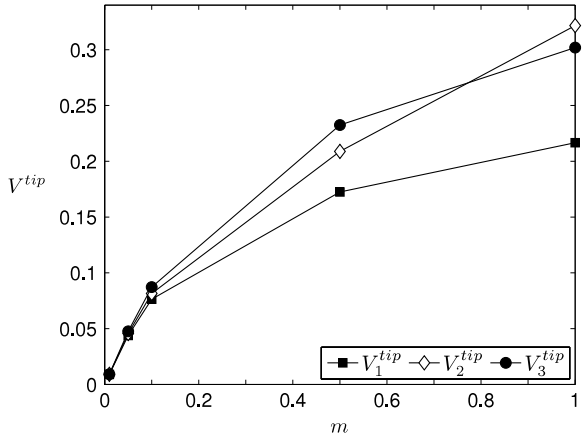

Fig. 7. Front velocities V_1^{tip}, V_2^{tip}, and V_3^{tip} as a function of the parameter m for $\theta = 30^\circ$, $Re = 3000$, and $We = \infty$.

4.2. Buoyancy-driven mixing of four-component fluids in two-dimensional tilted channels

Unless otherwise specified, we take the initial data as

$$c_1(x, y, 0) = \frac{1}{2}\left(1 + \tanh\left(\frac{x - 7.5}{2\sqrt{2}\epsilon}\right)\right),$$

$$c_2(x, y, 0) = \frac{1}{2}\left(\tanh\left(\frac{x - 5}{2\sqrt{2}\epsilon}\right) - \tanh\left(\frac{x - 7.5}{2\sqrt{2}\epsilon}\right)\right),$$

$$c_3(x, y, 0) = \frac{1}{2}\left(\tanh\left(\frac{x - 2.5}{2\sqrt{2}\epsilon}\right) - \tanh\left(\frac{x - 5}{2\sqrt{2}\epsilon}\right)\right),$$

$$u(x, y, 0) = v(x, y, 0) = 0$$

on the domain $\Omega = [0, 10] \times [0, 1]$, and use $h = 1/64$, $\Delta t = 0.128h$, and $\epsilon = 0.006\sqrt{2}$. We define V_k^{tip} as the front velocity of fluid k for $k = 1, 2, 3$.

Figs. 5, 6, 8, 10, 12 and 13 were created using the "contourf" command in MATLAB. In these figures, fluids 1, 2, 3, and 4 are represented by black, dark gray, gray, and white, respectively. To obtain the color contrast of each fluid, we shift the value of the phase-field variable by adding a constant, and take the contour of each different level. The following MATLAB code was used to create the figures: `hold all;contourf(C1,[0.5 0.5]);contourf (C2+1,[1.5 1.5]);contourf(C3+2,[2.5 2.5]); contourf(C4+3,[3.5 3.5]);colormap gray`.

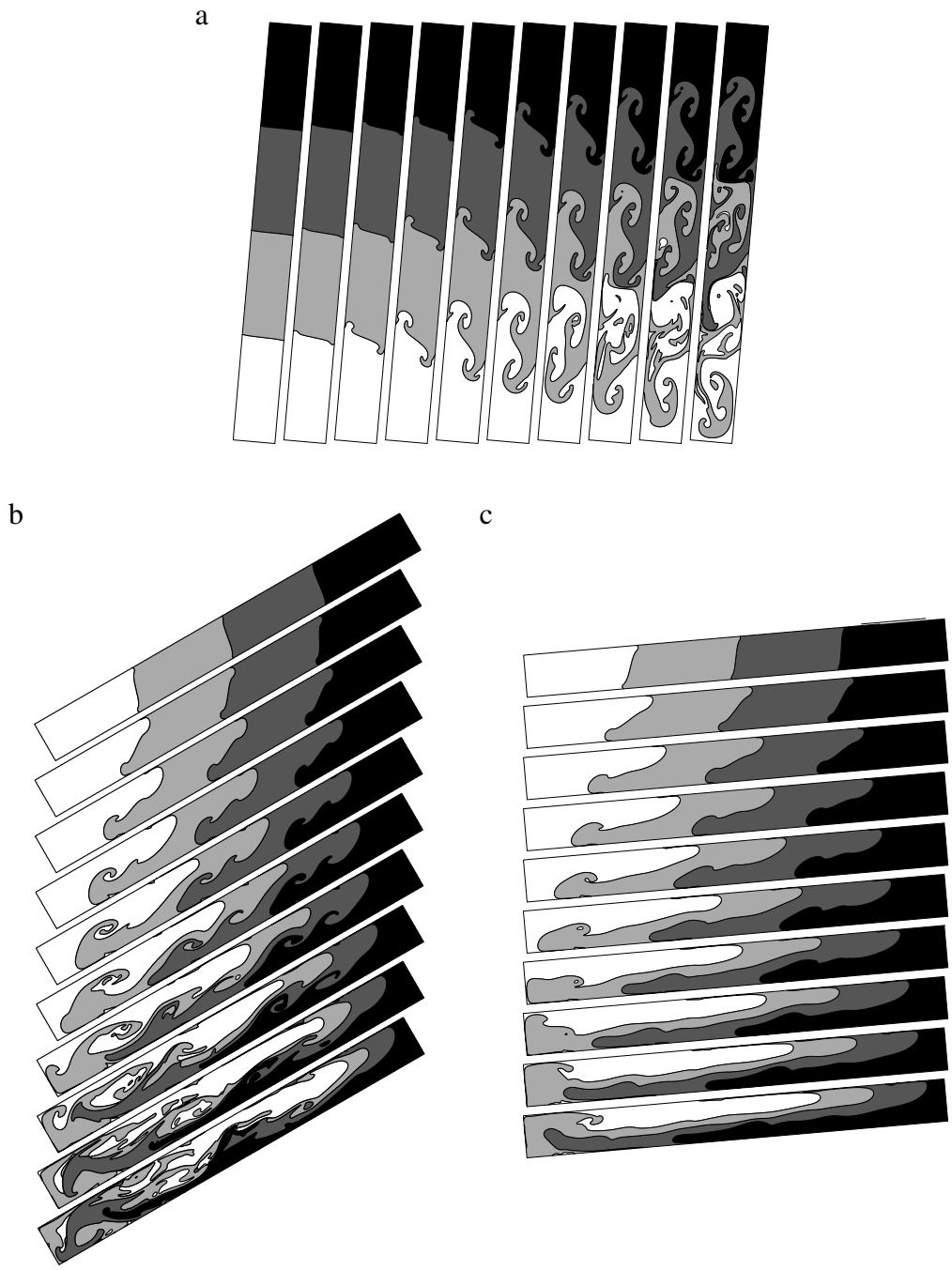

Fig. 8. Effect of tilt angle on the evolution of four-component fluids for (a) $\theta = 5^\circ$, (b) $\theta = 60^\circ$, and (c) $\theta = 85^\circ$. The other parameters are $m = 1$, $Re = 3000$, and $We = \infty$. The times are $t = 1, 2, 3, 4, 5, 6, 7, 8, 9$, and 10 (in (a), from left to right and, in (b) and (c), from top to bottom). Fluids 1, 2, 3, and 4 are represented by black, dark gray, gray, and white, respectively.

4.2.1. Effect of Péclet number

The Péclet number is the ratio between convective and diffusive mass transport. In order to examine the effect of the Péclet number on the interface profile, we consider the evolution of the interface with different Péclet numbers. The initial configuration is shown in Fig. 5(a), where $\theta = 30^\circ$, $\rho_1 : \rho_2 : \rho_3 : \rho_4 = 4 : 3 : 2 : 1$, $Re = 3000$, and $We = \infty$. Fig. 5(b)–(d) show snapshots of the interface profile at $t = 4$ for $Pe = 0.01/\epsilon$, $1/\epsilon$, and $100/\epsilon$, respectively. Next to each figure, the magnification shows the contour lines of the phase-field c_2 at levels 0.1, 0.2, . . . , 0.9.

$Pe = 0.01/\epsilon$ is small, and the diffusion term in the phase-field equation is dominant (Fig. 5(b)). Ideally, we want to minimize the diffusion effect of the phase-field, because we are primarily interested in the hydrodynamics of the multiphase system. Next, let us consider the other extreme case. $Pe = 100/\epsilon$ is relatively large, and the advection term in the phase-field equation is dominant. This implies that the interfaces are locally out of equilibrium. In Fig. 5(d), it can clearly be observed that the interfacial transition region is not smooth. The interface evolution is sensitive to the value of the Péclet number. Increasing the Péclet number results in a non-smooth concentration profile, whereas decreasing the Péclet number results in too much diffusion. On the other hand, if an appropriate Péclet number ($Pe = 1/\epsilon$) is taken, as in Fig. 5(c), we have both a smooth interfacial transition and complex interface profile according to the flow field. Unless otherwise stated, we use $Pe = 1/\epsilon$ throughout the rest of this paper.

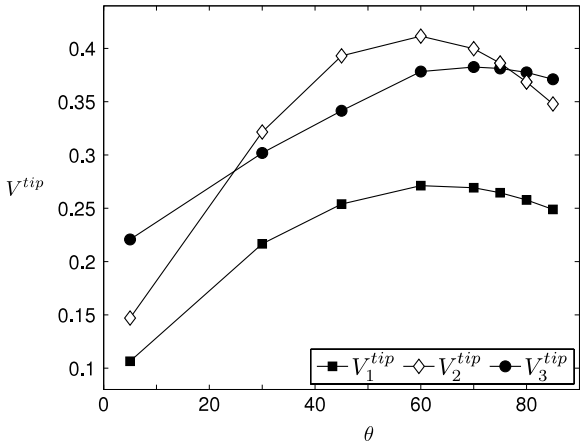

Fig. 9. Variation of V_1^{tip}, V_2^{tip}, and V_3^{tip} with $\theta = 5°$, 30°, 45°, 60°, 70°, 75°, 80°, and 85° for $m = 1$, $Re = 3000$, and $We = \infty$.

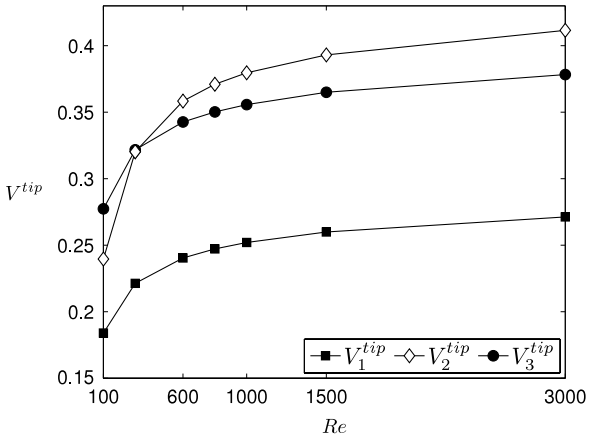

Fig. 11. Plot of the front velocities V_1^{tip}, V_2^{tip}, and V_3^{tip} against $Re = 100$, 300, 600, 800, 1000, 1500, and 3000. $\theta = 60°$, $m = 1$, and $We = \infty$ are used.

4.2.2. Effect of density ratio

In this section, we investigate the effect of the density ratio on the mixing dynamics for $\theta = 30°$, $Re = 3000$, and $We = \infty$. We take the density ratio between the four-component fluids to be $\rho_1 : \rho_2 : \rho_3 : \rho_4 = (1+3m) : (1+2m) : (1+m) : 1$ for some parameter m. The buoyancy force is proportional to the density, $\rho(\mathbf{c}) = \sum_{k=1}^{4} \rho_k c_k/\rho_4 = 3mc_1 + 2mc_2 + mc_3 + 1$. Therefore, as m increases (decreases), the buoyancy force acts more strongly (weakly).

Fig. 6(a)–(c) show the evolution of four-component fluids for $m = 0.1$, 0.5, and 1, respectively. The front velocities V_1^{tip}, V_2^{tip}, and V_3^{tip} for $m = 0.01$, 0.05, 0.1, 0.5, and 1 are shown in Fig. 7. At $m = 0.01$, V_1^{tip} (=0.0089), V_2^{tip} (=0.009), and V_3^{tip} (= 0.0091) are almost the same. As a result, the fronts of fluids 1, 2, and 3 move with an almost identical shape, and the interfaces are relatively simple. However, as the parameter m increases, the difference between V_1^{tip}, V_2^{tip}, and V_3^{tip} increases, and thus the formation of Kelvin–Helmholtz (KH) instabilities and small-scale structures increases. These instabilities and "roll-up" phenomena promote mixing in the four-component fluids. These trends are in agreement with the previous experiments of Séon et al. [7–11] and the computations of Sahu and Vanka [15].

4.2.3. Effect of tilt angle

At a fixed density ratio, the buoyancy force depends on the tilt angle, θ, of the channel. The axial component of the buoyancy force (proportional to $\cos\theta$) induces an axial interpenetration of the fluids. On the other hand, the transverse component of the buoyancy force (proportional to $\sin\theta$) acts to segregate the fluids. Therefore, the tilt angle plays a crucial role in determining the flow pattern and front velocity. In [8,9], Séon et al. found that, for θ between approximately 0° and 60°, the KH instabilities grow along the interface between the two-component fluids, enabling a strong transverse mixing. When the tilt angle was set to between approximately 60° and 80°, the transverse component of the buoyancy force started to act, increasing the segregation effects. We simulate tilt angles of $\theta = 5°$, 30°, 45°, 60°, 70°, 75°, 80°, and 85°.

For $m = 1$, $Re = 3000$, and $We = \infty$, Fig. 8(a)–(c) show the evolution of four-component fluids for $\theta = 5°$, 60°, and 85°, respectively. At low angles, the axial buoyancy force acts more strongly than the transverse buoyancy force. Thus, the KH instabilities develop along the interfaces, resulting in transverse interpenetration of the fluids. At high angles (including a nearly horizontal position), the transverse buoyancy force acts more strongly than the axial buoyancy force. This induces segregation between the four-component fluids, and interpenetration in the transverse direction decreases (Fig. 8(c)). The four-component fluids move parallel to each other, and the lighter (heavier) fluids move preferentially toward the upper (lower) part of the channel. The variation of V_1^{tip}, V_2^{tip}, and V_3^{tip} for $\theta = 5°$, 30°, 45°, 60°, 70°, 75°, 80°, and 85° is shown in Fig. 9. For fluid 1 and fluid 3, V_1^{tip} and V_3^{tip} increase with θ until they attain their maximum values, and then decrease gradually. However, in the case of fluid 2, V_2^{tip} decreases sharply after reaching its maximum value.

4.2.4. Effect of Reynolds number

Next, we study the effect of the Reynolds number on the mixing dynamics. Numerical experiments are carried out at several Reynolds numbers with $\theta = 60°$, $m = 1$, and $We = \infty$. Fig. 10 shows a snapshot of the interface profile of four-component fluids at $t = 6$ for $Re = 100$, 300, 600, 800, 1000, 1500, and 3000 (from second left to right) together with the initial configuration (left).

The results indicate that, as the Reynolds number increases (i.e., as the fluid viscosity decreases), the KH instabilities develop rapidly, mixing the four-component fluids transversally and leading to complex flow patterns. The front velocities V_1^{tip}, V_2^{tip}, and V_3^{tip} at $Re = 100$, 300, 600, 800, 1000, 1500, and 3000 are shown in

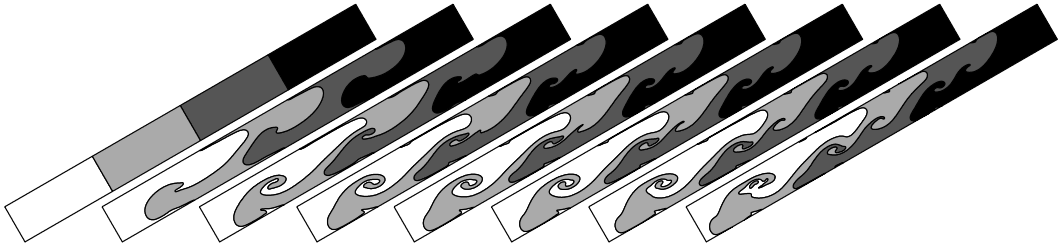

Fig. 10. Left is the initial configuration. Snapshots of the interface profile of four-component fluids at $t = 6$ for $Re = 100$, 300, 600, 800, 1000, 1500, and 3000 (from second left to right). $\theta = 60°$, $m = 1$, and $We = \infty$ are used. Fluids 1, 2, 3, and 4 are represented by black, dark gray, gray, and white, respectively.

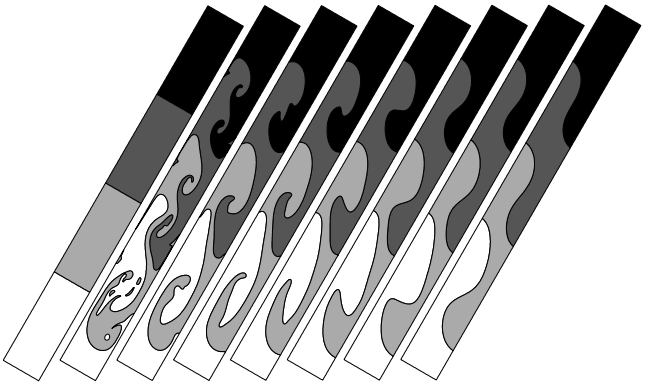

Fig. 12. Left is the initial configuration. Snapshots of the interface profile of four-component fluids at $t = 6$ for $We = \infty$, 100, 50, 20, 10, 7, and 5 (from second left to right). $\theta = 30^\circ$, $m = 1$, and $Re = 3000$ are used. Fluids 1, 2, 3, and 4 are represented by black, dark gray, gray, and white, respectively.

Fig. 11. An increase in the Reynolds number causes V_1^{tip}, V_2^{tip}, and V_3^{tip} to increase. Note that Sahu and Vanka [15] did not observe this at the high Atwood number ($At = (\rho_h - \rho_l)/(\rho_h + \rho_l)$, where ρ_h and ρ_l are the densities of the heavier and lighter fluids, respectively) studied in their simulations.

4.2.5. Effect of Weber number

We examine the effect of the Weber number on the mixing dynamics. Numerical experiments are carried out at several Weber numbers with $\theta = 30^\circ$, $m = 1$, and $Re = 3000$. Fig. 12 shows snapshots of the interface profile of four-component fluids at $t = 6$ for $We = \infty$, 100, 50, 20, 10, 7, and 5 (from second left to right), together with the initial configuration (left).

In the absence of surface tension ($We = \infty$), the waves of smaller wavelength grow with time and, as a result, the mixing of the four-component fluids becomes more vigorous. Note that, in the case of Newtonian fluids, the growth rate of the waves of smaller wavelength is small compared with the stabilizing effect of surface tension [45]. As we can see in Fig. 12, the stabilizing influence increases as the Weber number decreases (as the surface tension coefficient increases). It can be seen that surface tension stabilizes short-wavelength disturbances.

4.2.6. Effect of the aspect ratio of a tilted channel

In order to examine the effect of the channel aspect ratio on the mixing dynamics, we consider the evolution of the interface with different channel aspect ratios with $\theta = 30^\circ$, $m = 1$, $Re = 3000$, and $We = \infty$. Fig. 13(a), (b) and (c) show the evolution of four-component fluids for $H : L = 1 : 10, 2 : 10$, and $4 : 10$, respectively. In a horizontal narrow channel (small H), the wall effect becomes more significant. In our simulations, we impose the no-slip boundary condition ($\mathbf{u} = \mathbf{0}$ on $\partial\Omega$) for velocities at the walls. At small H (=1), velocities on the inside of the tilted channel are more affected by the no-slip boundary condition. As a result, we can see relatively slow four-component fluid flows (Fig. 13(a)). In contrast, at large H (=4), relatively fast velocity fields are formed, causing the fluids to move to the left wall ($x = 0$) within a shorter time (Fig. 13(c)).

4.2.7. Comparison between the mixing of two- and four-component fluids with the same maximum density contrast

We now compare the buoyancy-driven mixing of two- and four-component fluids with the same maximum density contrast. For the two- and four-component fluids, we respectively take the initial data as

$$c(x, y, 0) = \frac{1}{2}\left(1 + \tanh\left(\frac{x - 20}{2\sqrt{2}\epsilon}\right)\right)$$

and

$$c_1(x, y, 0) = \frac{1}{2}\left(1 + \tanh\left(\frac{x - 30}{2\sqrt{2}\epsilon}\right)\right),$$

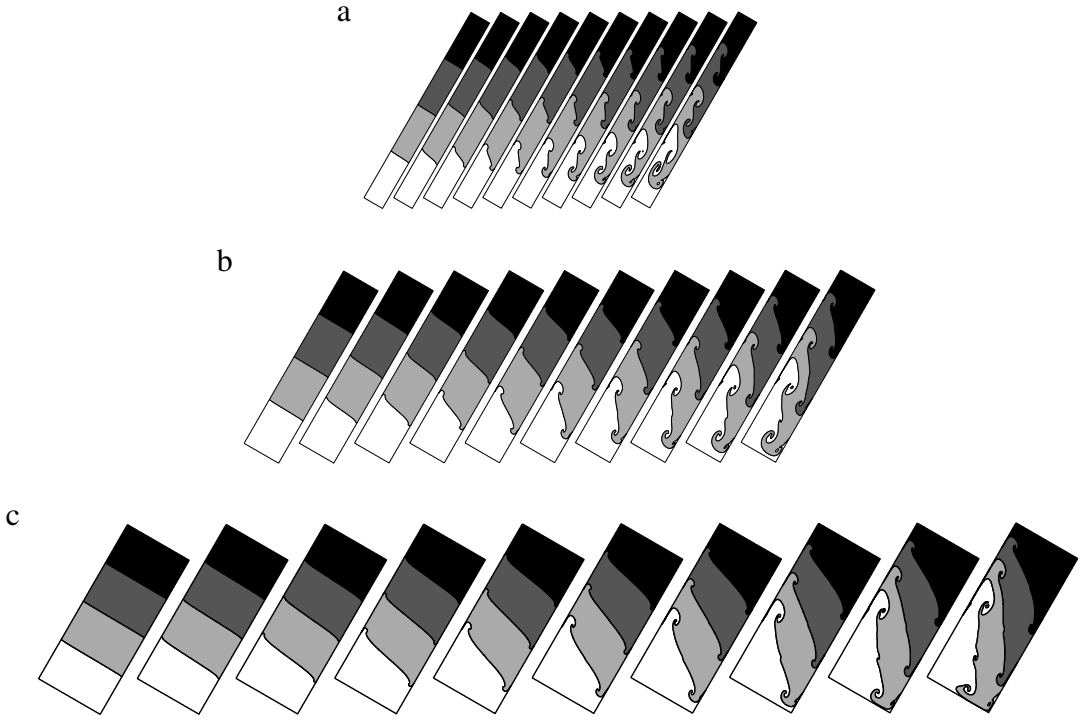

Fig. 13. Effect of channel aspect ratio on the evolution of four-component fluids for (a) $H : L = 1 : 10$, (b) $H : L = 2 : 10$, and (c) $H : L = 4 : 10$. The other parameters are $\theta = 30^\circ$, $m = 1$, $Re = 3000$, and $We = \infty$. The times are $t = 0.5$, 1, 1.5, 2, 2.5, 3, 3.5, 4, 4.5, and 5 (from left to right). Fluids 1, 2, 3, and 4 are represented by black, dark gray, gray, and white, respectively.

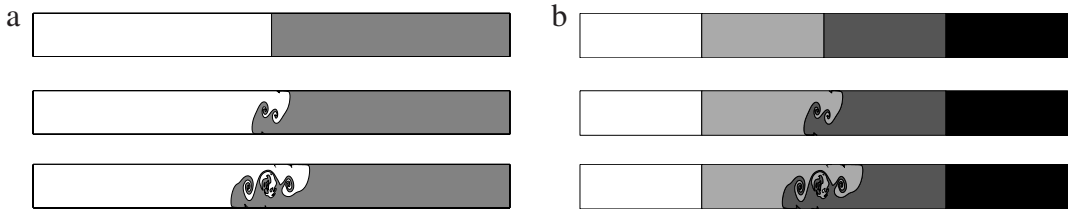

Fig. 14. Comparison between the mixing of (a) two- and (b) four-component fluids with the same maximum density contrast. In these tests, the maximum density contrast is 1.2. In both cases, $\theta = 60^\circ$, $Re = 558.6$, and $We = \infty$. The top, middle, and bottom rows show the results at $t = 0$, 10, and 20, respectively.

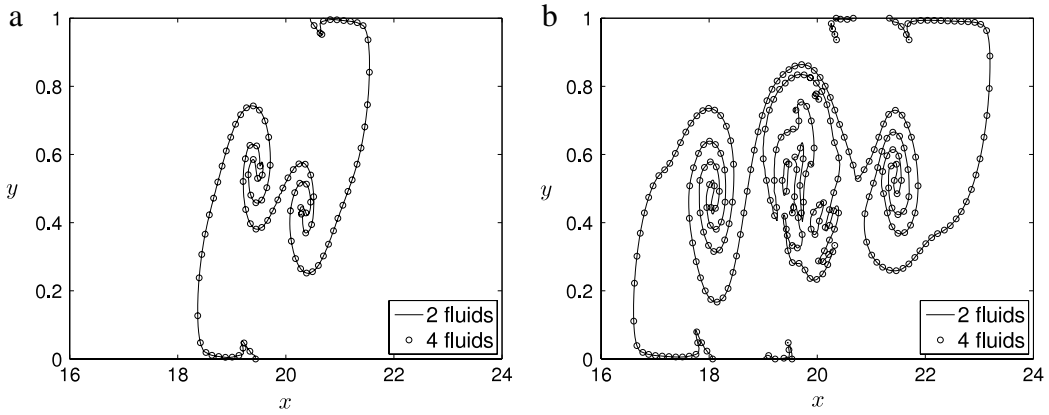

Fig. 15. Contours of the phase-fields on $[16, 24] \times [0, 1]$ at (a) $t = 10$ and (b) $t = 20$. In each figure, the solid line and open circles show the contours of the phase-fields for two- and four-component fluids, respectively.

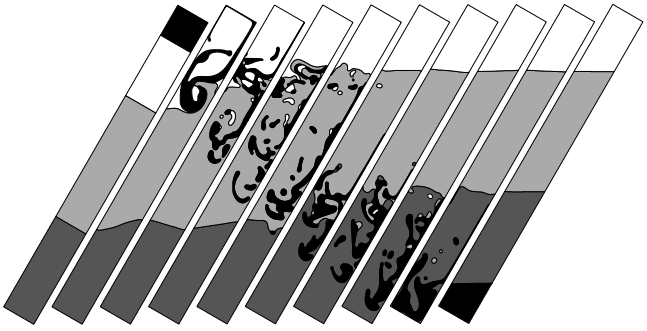

Fig. 16. Buoyancy-driven mixing of initially partly stable configurations. The computational domain is $\Omega = [0, 10] \times [0, 1]$, and $h = 1/64$, $\Delta t = 0.128h$, $\epsilon = 0.006\sqrt{2}$, $Pe = 0.1/\epsilon$, $\theta = 30^\circ$, $\rho_1 : \rho_2 : \rho_3 : \rho_4 = 4 : 1 : 2 : 3$, $Re = 3000$, and $We = \infty$. The times are $t = 0$, 5, 10, 15, 20, 30, 35, 40, 50, and 100 (from left to right). Fluids 1, 2, 3, and 4 are represented by black, white, gray, and dark gray, respectively.

$$c_2(x, y, 0) = \frac{1}{2}\left(\tanh\left(\frac{x-20}{2\sqrt{2}\epsilon}\right) - \tanh\left(\frac{x-30}{2\sqrt{2}\epsilon}\right)\right),$$

$$c_3(x, y, 0) = \frac{1}{2}\left(\tanh\left(\frac{x-10}{2\sqrt{2}\epsilon}\right) - \tanh\left(\frac{x-20}{2\sqrt{2}\epsilon}\right)\right).$$

In both cases, the initial velocity is zero, the computational domain is $\Omega = [0, 40] \times [0, 1]$, and we choose $h = 1/64$, $\Delta t = 0.128h$, $\theta = 60^\circ$, $Re = 558.6$, and $We = \infty$. For the two-component fluids, the other parameters are $\epsilon = 0.01\sqrt{2}$, $Pe = 100/\epsilon$, and $\rho_1/\rho_2 = 1.2$, and for the four-component fluids we select parameter values of $\epsilon = 0.006\sqrt{2}$, $Pe = 100/\epsilon$, and $\rho_1 : \rho_2 : \rho_3 : \rho_4 = 1.2 : 1.2 : 1 : 1$. We match the maximum density contrast for both cases. Fig. 14(a) and (b) show the evolution of two- and four-component fluids at the same times, respectively. The top, middle, and bottom rows show the results at $t = 0$, 10, and 20, respectively. The contours of the phase-fields on $[16, 24] \times [0, 1]$ at $t = 10$ and 20 are shown in Fig. 15(a) and (b), respectively. In each figure, the solid line and open circles show the contours for the two- and four-component fluids, respectively. Initially, for both cases, the densities in the left and right halves of the domain are 1 and 1.2, respectively. Thus, the velocity fields in each half of the domain are the same in both cases, and the phase-fields in each half of the domain are convected by the same velocity. As a result, both the two- and four-component fluids with the same maximum density contrast yield nearly identical phase-field evolutions.

4.2.8. Mixing of initially partly stable four-component fluids

We now investigate the buoyancy-driven mixing of initially partly stable configurations with both stable and unstable stratifications. The initial configuration is shown on the left of Fig. 16. Fluids 1, 2, 3, and 4 are represented by black, white, gray, and dark gray, respectively. The computational domain is $\Omega = [0, 10] \times [0, 1]$, and $h = 1/64$, $\Delta t = 0.128h$, $\epsilon = 0.006\sqrt{2}$, $Pe = 0.1/\epsilon$, $\theta = 30^\circ$, $\rho_1 : \rho_2 : \rho_3 : \rho_4 = 4 : 1 : 2 : 3$, $Re = 3000$, and $We = \infty$. Fig. 16 shows the evolution of four-component fluids. Due to the given density contrast, fluids 2, 3, and 4 form stable layers, and thus there is almost no change in position between these fluids. However, the heaviest fluid (fluid 1) is on top of the other fluids and, in turn, moves to the bottom of other fluids due to the gravitational force. After $t = 20$, 40, and 60, fluid 1 (shown in black) is below fluid 2 (in white), fluid 3 (in gray), and fluid 4 (in dark gray), respectively. Finally, after $t = 100$, the system reaches an equilibrium state: heavier fluids lie below lighter fluids, and the interfaces are flat and perpendicular to the gravitational direction.

5. Conclusions

The buoyancy-driven mixing of multi-component incompressible immiscible fluids in two-dimensional tilted channels was studied numerically using a phase-field model. The mixing dynamics are governed by the modified Navier–Stokes equations and the multi-component convective Cahn–Hilliard equations. A finite difference method was used to solve the governing system. To solve the equations efficiently and accurately, we employed the

Chorin's projection method for the modified Navier–Stokes equations, and the recently developed practically unconditionally stable method for the multi-component Cahn–Hilliard equations. We numerically investigated the effects of various density ratios, tilt angles, Reynolds numbers, and Weber numbers on the interface structures and front velocities. The trends observed in simulations with multi-component fluids were consistent with previous experimental and numerical results with two-component fluids.

Acknowledgments

The first author (Hyun Geun Lee) was supported by Basic Science Research Program through the National Research Foundation of Korea (NRF) funded by the Ministry of Education, Science and Technology (2012R1A6A3A01019827). The authors greatly appreciate the reviewers for their constructive comments and suggestions, which improved the quality of this paper. The corresponding author (J.S. Kim) also thanks Dr. Lee for suggesting this problem and for valuable discussions.

References

[1] T.B. Benjamin, Gravity currents and related phenomena, J. Fluid Mech. 31 (1968) 209–248.
[2] M.H.I. Baird, K. Aravamudan, N.V.R. Rao, J. Chadam, A.P. Peirce, Unsteady axial mixing by natural convection in a vertical column, AIChE J. 38 (1992) 1825–1834.
[3] J.E. Simpson, Gravity Currents in the Environment and the Laboratory, second ed., Cambridge University Press, Cambridge, 1997.
[4] D.D. Joseph, R. Bai, K.P. Chen, Y.Y. Renardy, Core-annular flows, Annu. Rev. Fluid Mech. 29 (1997) 65–90.
[5] E.E. Zukoski, A review of flows driven by natural convection in adiabatic shafts, NIST Report No. NIST-GCR-95-679, US Department of Commerce, USA, 1995.
[6] Q. Cao, A.L. Ventresca, K.R. Sreenivas, A.K. Prasad, Instability due to viscosity stratification downstream of a centreline injector, Can. J. Chem. Eng. 81 (2003) 913–922.
[7] T. Séon, J.-P. Hulin, D. Salin, B. Perrin, E.J. Hinch, Buoyant mixing of miscible fluids in tilted tubes, Phys. Fluids 16 (2004) L103.
[8] T. Séon, J.-P. Hulin, D. Salin, B. Perrin, E.J. Hinch, Buoyancy driven miscible front dynamics in tilted tubes, Phys. Fluids 17 (2005) 031702.
[9] T. Séon, J.-P. Hulin, D. Salin, B. Perrin, E.J. Hinch, Laser-induced fluorescence measurements of buoyancy driven mixing in tilted tubes, Phys. Fluids 18 (2006) 041701.
[10] T. Séon, J. Znaien, D. Salin, J.P. Hulin, E.J. Hinch, B. Perrin, Transient buoyancy-driven front dynamics in nearly horizontal tubes, Phys. Fluids 19 (2007) 123603.
[11] T. Séon, J. Znaien, B. Perrin, E.J. Hinch, D. Salin, J.P. Hulin, Front dynamics and macroscopic diffusion in buoyant mixing in a tilted tube, Phys. Fluids 19 (2007) 125105.
[12] S.M. Taghavi, T. Séon, D.M. Martinez, I.A. Frigaard, Influence of an imposed flow on the stability of a gravity current in a near horizontal duct, Phys. Fluids 22 (2010) 031702.
[13] Y. Hallez, J. Magnaudet, Effects of channel geometry on buoyancy-driven mixing, Phys. Fluids 20 (2008) 053306.
[14] K.C. Sahu, H. Ding, P. Valluri, O.K. Matar, Pressure-driven miscible two-fluid channel flow with density gradients, Phys. Fluids 21 (2009) 043603.
[15] K.C. Sahu, S.P. Vanka, A multiphase lattice Boltzmann study of buoyancy-induced mixing in a tilted channel, Comput. Fluids 50 (2011) 199–215.
[16] P.R. Redapangu, S.P. Vanka, K.C. Sahu, Multiphase lattice Boltzmann simulations of buoyancy-induced flow of two immiscible fluids with different viscosities, Eur. J. Mech. B Fluids 34 (2012) 105–114.
[17] J.O. Shin, S.B. Dalziel, P.F. Linden, Gravity currents produced by lock exchange, J. Fluid Mech. 521 (2004) 1–34.
[18] A. Ghasemi, B. Firoozabadi, M. Mahdinia, 2D numerical simulation of density currents using the SPH projection method, Eur. J. Mech. B Fluids 38 (2013) 38–46.
[19] V.E. Badalassi, H.D. Ceniceros, S. Banerjee, Computation of multiphase systems with phase field models, J. Comput. Phys. 190 (2003) 371–397.
[20] F. Boyer, L. Chupin, P. Fabrie, Numerical study of viscoelastic mixtures through a Cahn–Hilliard flow model, Eur. J. Mech. B Fluids 23 (2004) 759–780.
[21] J. Kim, J. Lowengrub, Phase field modeling and simulation of three-phase flows, Interfaces Free Bound. 7 (2005) 435–466.
[22] F. Boyer, C. Lapuerta, Study of a three component Cahn–Hilliard flow model, ESAIM Math. Model. Numer. Anal. 40 (2006) 653–687.
[23] J. Kim, Phase field computations for ternary fluid flows, Comput. Methods Appl. Mech. Engrg. 196 (2007) 4779–4788.
[24] J. Kim, A generalized continuous surface tension force formulation for phase-field models for multi-component immiscible fluid flows, Comput. Methods Appl. Mech. Engrg. 198 (2009) 3105–3112.
[25] F. Boyer, S. Minjeaud, Numerical schemes for a three component Cahn–Hilliard model, ESAIM Math. Model. Numer. Anal. 45 (2011) 697–738.
[26] H.G. Lee, J.-W. Choi, J. Kim, A practically unconditionally gradient stable scheme for the N-component Cahn–Hilliard system, Physica A 391 (2012) 1009–1019.
[27] A.J. Chorin, A numerical method for solving incompressible viscous flow problems, J. Comput. Phys. 2 (1967) 12–26.
[28] H. Ding, P.D.M. Spelt, C. Shu, Diffuse interface model for incompressible two-phase flows with large density ratios, J. Comput. Phys. 226 (2007) 2078–2095.
[29] J.W. Cahn, C.M. Elliott, A. Novick-Cohen, The Cahn–Hilliard equation with a concentration dependent mobility: motion by minus the Laplacian of the mean curvature, European J. Appl. Math. 7 (1996) 287–301.
[30] C.M. Elliott, H. Garcke, On the Cahn–Hilliard equation with degenerate mobility, SIAM J. Math. Anal. 27 (1996) 404–423.
[31] J. Zhu, L.-Q. Chen, J. Shen, V. Tikare, Coarsening kinetics from a variable-mobility Cahn–Hilliard equation: Application of a semi-implicit Fourier spectral method, Phys. Rev. E 60 (1999) 3564–3572.
[32] D. Kay, R. Welford, A multigrid finite element solver for the Cahn–Hilliard equation, J. Comput. Phys. 212 (2006) 288–304.
[33] J. Kim, A numerical method for the Cahn–Hilliard equation with a variable mobility, Commun. Nonlinear Sci. Numer. Simul. 12 (2007) 1560–1571.
[34] H.G. Lee, J. Kim, A second-order accurate non-linear difference scheme for the N-component Cahn–Hilliard system, Physica A 387 (2008) 4787–4799.
[35] R. Toral, A. Chakrabarti, J.D. Gunton, Numerical study of the Cahn–Hilliard equation in three dimensions, Phys. Rev. Lett. 60 (1988) 2311–2314.
[36] D.J. Eyre, An unconditionally stable one-step scheme for gradient systems. Preprint, 1998.
[37] X. Feng, A. Prohl, Numerical analysis of the Cahn–Hilliard equation and approximation of the Hele-Shaw problem, Interfaces Free Bound. 7 (2005) 1–28.
[38] E.V.L. de Mello, O. Teixeira da Silveira Filho, Numerical study of the Cahn–Hilliard equation in one, two and three dimensions, Physica A 347 (2005) 429–443.
[39] H.D. Ceniceros, A.M. Roma, A nonstiff, adaptive mesh refinement-based method for the Cahn–Hilliard equation, J. Comput. Phys. 225 (2007) 1849–1862.
[40] W.M. Feng, P. Yu, S.Y. Hu, Z.K. Liu, Q. Du, L.Q. Chen, A Fourier spectral moving mesh method for the Cahn–Hilliard equation with elasticity, Commun. Comput. Phys. 5 (2009) 582–599.
[41] H.G. Lee, J. Kim, Accurate contact angle boundary conditions for the Cahn–Hilliard equations, Comput. Fluids 44 (2011) 178–186.
[42] H.G. Lee, K.M. Kim, J. Kim, On the long time simulation of the Rayleigh–Taylor instability, Internat. J. Numer. Methods Engrg. 85 (2011) 1633–1647.
[43] F.H. Harlow, J.E. Welch, Numerical calculation of time-dependent viscous incompressible flow of fluid with free surface, Phys. Fluids 8 (1965) 2182–2189.
[44] U. Trottenberg, C. Oosterlee, A. Schüller, Multigrid, Academic Press, London, 2001.
[45] Y. Renardy, Stability of the interface in two-layer Couette flow of upper convected Maxwell liquids, J. Non-Newton. Fluid Mech. 28 (1988) 99–115.